Quasi-common path three-wavelength holographic interferometer based on Wollaston prisms

Jean-Michel Desse, Pascal Picart

Quasi-common path three-wavelength holographic interferometer based on Wollaston prisms

Jean-Michel Desse [a,*], Pascal Picart [b]

[a] ONERA, The French Aerospace Lab, 5, Boulevard Paul Painlevé, 59045 Lille, France
[b] Université du Maine, CNRS UMR 6613, LAUM, Av. Olivier Messiaen, 72085 Le Mans Cedex 9, France

This article presents a digital three-wavelength holographic interferometer based on the use of two Wollaston prisms. This provides an in-line setup with quasi common-path and as a consequence there is no additional independent reference wave to be added. Thus, immunity to external perturbations such as vibrations or thermal perturbations is achieved. Furthermore, the set-up exhibits a single shot and real time capability which is very useful to study dynamic events. By using the two Wollaston prisms in an astigmatic configuration, spatial carrier frequencies can be adjusted both in amplitude and orientation. The digital hologram processing is based on Fourier processing and filtering around the carrier spatial frequency so that phase shifting is not required. The use of three wavelengths leads to visualizing directly the zero order fringe and regions for which there is no air density variation in a dynamic flow. Experimental proof of concept is demonstrated with a supersonic jet when the injection pressure varies.

1. Introduction

In the past decade, phase imaging has developed at an accelerating pace and impacted a wide range of domains, such as microscopy (also known as quantitative phase imaging or interferometric phase microscopy) [1–15], fluid mechanics [16–18], or photomechanics [19–23]. Phase imaging measures the optical path length map associated with transparent specimens (transmission illumination) or opaque surfaces (reflection illumination) and translates this data into relevant information. In such a way, biomedical imaging [7,8,10,11], topology at nanoscale [9,19], flows and vortices [16,17], material properties [19], surface shape [20], polarization imaging [21], displacement field [22,23], vibrations [24–27], particles tracking [28–31], measurement of temperatures or thermal exchanges in flames [32,33] were investigated. Off-axis methods provide the fastest acquisition rates, because the phase information is extracted from a single recorded hologram. As a general rule, phase extraction from in-line holograms is performed with phase-shifting [34]. In off-axis digital holography, the reference wave is shaped to provide a spatial separation in the reconstruction plane or in the Fourier plane of the hologram (slight tilt) [1,16,35,36]. Tilting the object and reference waves (i.e. adding a spatial carrier frequency to the hologram) can be performed according many different ways: tilting one mirror in a Michelson [1,10,16] or a Mach-Zehnder interferometer [19,24], using a Lloyd mirror [4], or using a diffraction grating associated to a spatial filtering [5,7,9]. A Michelson set-up is quite easy to implement and to experimentally adjust. In that case, the transparent object is crossed twice by the probe beam. Thus, the measurement sensitivity is two times that of a Mach-Zehnder and that can be very advantageous for weak phase changes. However, if the object exhibits high density gradients, a shadow effect may be superimposed on the hologram fringes, thus reducing their visibility. As a common feature, in a Michelson and a Mach-Zehnder set-up, the optical paths are quite different. When using a diffraction gating, the optical paths are quasi-common, but the filtering induces losses which reduce the light efficiency of the set-up. Note that the use of an independent reference wave induces sensitivity to external perturbations such as vibrations, temperature changes, etc., and leads to an increase in the set-up complexity. So as to get a reference wave removed or quite commons optical paths, the pure in-line configuration is well adapted [15,30], but the faculty for a direct phase contrast recovering has to be developed.

The use of multiple wavelengths in digital holography was initially proposed by Yamaguchi [37,38]. At the same time, Demoli presented the first study on fluids using digital color Fourier holography using a monochrome sensor with a sequential recording of three laser wavelengths. Qualitative results were obtained to

* Corresponding author.
E-mail address: Jean-michel.Desse@onera.fr (J.-M. Desse).

visualize convective flows induced by the thermal dissipation in a tank filled with oil [39]. Quantitative results were obtained to analyze the variations in the refractive index induced by a candle flame [16] and for the gas density on a subsonic near wake flow downstream a circular cylinder [18]. The use of three different wavelengths is a powerful approach to determine the absolute zero order in the field of view. The absolute zero order is found by observing the synthesized color fringes whereas it cannot be found by considering the calculated unwrapped phase data. Indeed, each unwrapped phase map is obtained with an unknown value multiple of 2π. However, it can be found by considering the wrapped phase: the zero order fringe is that for which all the three wrapped phase values are identically null [16]. Since then, an increasing number of important applications have relied on the possibilities of using digital color holography to record and reconstruct colored objects at high precisions using a simple optical setup [40–56].

Thus, this article presents a digital three-wavelength holographic interferometer based on the use of two Wollaston prisms that aims at overcoming the major drawbacks of the previous techniques. The proposed set-up is based on a "Z" architecture and the use of two Wollaston prisms. This provides an in-line setup with quasi common-path and as a consequence there is no additional independent reference wave to be added and no losses in the light transmission. Thus, immunity to external perturbations such as vibrations or thermal perturbations is achieved. Furthermore, the set-up exhibits a single shot and real time capability that is quite useful to investigate high speed transient flows. The article is organized as follows: section 2 establishes the basic principle of the optical set-up and section 3 describes the digital hologram processing. In section 4, experimental results are provided and section 5 draws conclusions to this study.

2. Basic principle

2.1. Optical set-up

The optical set-up is described in Fig. 1 and is based on a "Z" configuration. The light source is constituted of three different DPSS lasers (660 nm, 532 nm and 457 nm). The beams are spatially filtered with a microscope objective associated to a micrometric pinhole. Then, the beams are extended and focused in the first large field Wollaston prism (8° angle). A linear polarizer is used to adjust the input polarization. The prism is localized at the focal point of a spherical mirror. The two beams emerging from the first Wollaston prism are orthogonally polarized. After reflection by the spherical mirror, the beams are parallel and one half of the expanded beam crosses the test section whereas the other one constitutes the reference beam. This configuration provides immunity to external perturbations such as vibrations or thermal perturbations. In addition, the "Z" configuration leads to a quite common-path holographic interferometer, having the capability of fully transmitting the light issued from the source to the sensor. After reflection on the second spherical mirror, the beams are focalized in the second first large field Wollaston prism. This second prism is mounted "upside down" with the first one. An analyzer is then placed behind the second prism in order to produce interferences between the orthogonally polarized beams. A lens localized in front of the camera creates the image of the test section at/or nearby the recording plane. The sensor is based on a 3CCD cooled digital color camera equipped with three CCD chips, including 1344×1024 pixels sized $6.45\ \mu m \times 6.45\ \mu m$. The colors are separated using a dichroic prism.

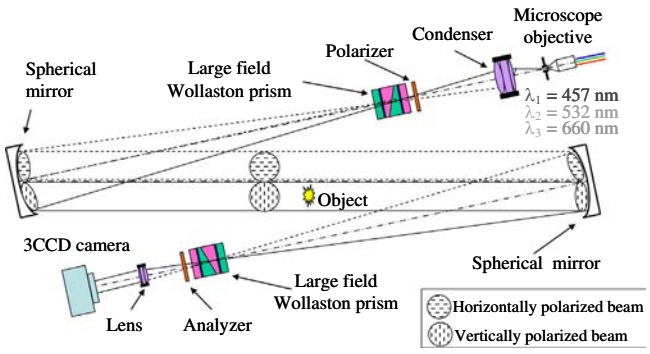

Fig. 1. Optical set-up with two Wollaston prisms in "Z" configuration.

2.2. Characteristics of the Wollaston prism

Large field Wollaston prisms which strongly separate the two interfering beams were designed. This means that each prism has to generate a distance between the two interfering beams that is greater than the dimension of the field of view to be measured. The hologram is constituted with two beams: the first one does not pass through the phenomenon (reference beam) and the second one crosses the phenomenon under interest (see Fig. 1). For a spherical mirror with diameter $D=250$ mm, a curvature radius $R=2.5$ m, the distance dx between the two interfering beams should be about 125 mm. If n_e and n_o are respectively the extraordinary and ordinary refractive index, $\Delta n = n_e - n_o$ is the crystal birefringence, α is the bonding angle of prism, then the birefringence angle ϵ is given by:

$$\epsilon = 2.\Delta n.tan(\alpha) \tag{1}$$

and dx can be expressed according to the following relationship:

$$dx = \epsilon.R = 2.R.\Delta n.\ \tan(\alpha) \tag{2}$$

By choosing calcite as material, the bonding angle is found to be:

$$\alpha = tan^{-1}\left(\frac{dx}{2.R.\Delta n}\right) = 8°27 \tag{3}$$

2.3. Astigmatic properties of the optical set-up

The "Z" optical path generates astigmatism because the two spherical mirrors work in an off-axis configuration. The first prism is located at the focal point of the first spherical mirror, so that the two optical rays which are reflected onto the second spherical mirror may be parallel. The second spherical mirror refocuses the light into the second Wollaston prism. Note that due to astigmatism in the set-up, the second focusing point in the front of the sensor is not unique. Fig. 2 illustrates how the optical beams are focused on the two small focal lines separated by a few millimeters along the optical axis. The first focal line is due to the focusing beam in the horizontal plane (tangential image), and the second one is the sagittal image, and it is due to beams focusing in the vertical plane. This particularity of the set-up leads to straight and parallel interference fringes in the field of view, i.e. the set-up includes in an automatic manner a set of spatial carrier frequencies. Fig. 3 illustrates this particular feature. Interference fringes are shown in Fig. 3, according, both to the position of the prism

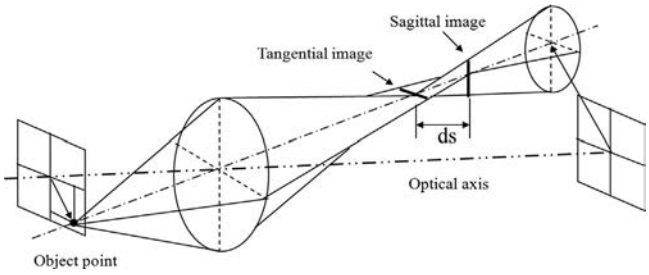

Fig. 2. Astigmatism represented by sectional views.

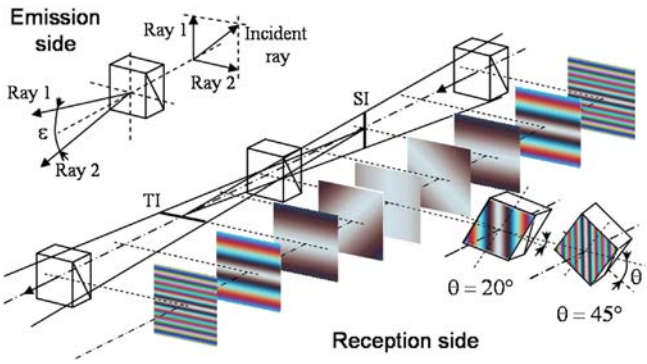

Fig. 3. Evolution of interference fringes when the second Wollaston is moved from the sagittal image to the tangential image.

and to the rotation angle of the prism relatively to the optical axis. For example, on the emission side, the three incident rays are polarized at 45° of the crystal axis and the first Wollaston prism is located so that the two interfering rays are split in a vertical plane. On the reception side, when the second Wollaston prism is successively moved along the optical axis towards the sagittal image (SI), the interferences fringes which were horizontal and much narrowed, spread. When the Wollaston prism is moved from the sagittal image (SI) to the tangential image (TI), the interference fringes spread again, but they rotate by 90° to give a quasi-uniform vertical background color, at half distance between the tangential and sagittal images. Then, they continue to rotate by 90° up to the sagittal image and they narrow to become horizontal. Above the sagittal image, interference fringes stay horizontal and narrow more and more. It follows that the spatial carrier frequency can be adjusted by the axial displacement of the prism for its amplitude and by rotating the prism for its orientation. In these experiments, the Wollaston prism is located at half distance between the tangential and sagittal images, because it generates interference fringes in the same direction as the direction of the two interfering beams (vertical shift and vertical fringes). This feature was described by Gontier [57]. To increase the number of fringes in the visualized field, the Wollaston prism has to be turned on itself in the plane perpendicular to the optical axis. Two positions are shown in Fig. 3 (20° and 45°) where one can see that the maximum number of fringes is obtained for a rotation of 45°.

3. Digital hologram processing

From the optical set-up and adjustment of the second Wollaston prism (see Fig. 3), digital color holograms including spatial carrier frequencies (off-axis holography) are recorded and processed. The introduction of the spatial carrier frequency by the Wollaston prism leads to the recording of one color hologram at each instant, since there is no need for phase shifting. This provided a single shot and real time capability to the experimental set-up to investigate high speed transient flows. For any wavelength λ, the recorded image plane hologram can be expressed as:

$$H_\lambda(x,y) = |O(x,y)|^2 + |R(x,y)|^2 + O^*(x,y)R(x,y) + O(x,y)R^*(x,y) \quad (4)$$

where $O(x,y)$ and $R(x,y)$ are the object and the reference wave respectively. For convenience $R(x,y)$ can be represented with unitary amplitude. By taking into account of the spatial carrier modulation introduced by the Wollaston prism, the hologram at wavelength λ can be written according to Eq. (5):

$$H_\lambda(x,y) = O_0(x,y) + O(x,y)\exp[2i\pi(u_\lambda x + v_\lambda y)] + O^*(x,y)\exp[-2i\pi(u_\lambda x + v_\lambda y)] \quad (5)$$

In Eq. (5), $2i\pi(u_\lambda x + v_\lambda y)$ is the spatial carrier modulation along the x-y coordinates of the set of reference axis, $O_0 = |O(x,y)|^2 + |R(x,y)|^2$ is the zero order diffraction and we consider $O = a_\lambda \exp(i\varphi_\lambda)$. Subscript λ refers to one of the three colors, i.e. λ=R, G or B. The Fourier transform of Eq. (5) leads to:

$$\tilde{H}_\lambda(u,v) = \tilde{O}_0(u,v) + \tilde{C}_\lambda(u-u_\lambda, v-v_\lambda) + \tilde{C}_\lambda^*(-u-u_\lambda, -v-v_\lambda) \quad (6)$$

where $\tilde{C}_\lambda$ and $\tilde{O}_0$ are respectively the Fourier transform of $C_\lambda = O\exp[2i\pi(u_\lambda x + v_\lambda y)]$ and O_0. If the spatial frequencies u_λ and v_λ are correctly adjusted, the three orders are well separated in the spatial frequency spectrum. By applying a bandwidth limited filter ($\Delta u \times \Delta v$ wide) around the spatial frequency (u_λ,v_λ), and after filtering and inverse 2D Fourier transform, one gets the object complex amplitude:

$$C_\lambda(x,y) \cong \{a_\lambda(x,y)\exp[i\phi_\lambda(x,y)]\exp[2i\pi(u_\lambda x + v_\lambda y)]\} * h(x,y) \quad (7)$$

where $*$ means convolution and $h(x,y)$ is the impulse response corresponding to the filtering applied in the Fourier domain. The impulse response is such that

$$h(x,y) = \Delta u \Delta v \exp[2i\pi(u_\lambda x + v_\lambda y)]\,\mathrm{sinc}(\pi\Delta u x)\,\mathrm{sinc}(\pi\Delta v y) \quad (8)$$

The spatial resolution is then related to $1/\Delta u$ and $1/\Delta v$ respectively in the x-y axis [16]. In addition the phase recovered with
Eq. (7) includes the spatial carrier modulation that has to be removed. This is achieved by multiplying C_λ by $\exp[-2i\pi(u_\lambda x + v_\lambda y)]$.

Note that if the image of the test section is not in focus, the refocusing can be performed using the angular spectrum transfer function to get an in-focus image [58]. After the reconstruction process, the optical phase can be estimated from relation (9):

$$\phi_\lambda(x,y) = \tan^{-1}\left(\frac{\Im_m[C_\lambda(x,y)]}{\Re_e[C_\lambda(x,y)]}\right) \quad (9)$$

and the amplitude at wavelength λ by:

$$a_\lambda(x,y) = \sqrt{\Im_m^2[C_\lambda(x,y)] + \Re_e^2[C_\lambda(x,y)]} \quad (10)$$

In Eq. (9,10), $\Im_m[...]$ and $\Re_e[...]$ mean imaginary and real part of complex value.

When the test section is modified, for example by heating or with a flow circulation, a refractive index variation is induced along the object beam, and this modifies the optical path and then the optical phase. The phase change $\Delta\varphi_\lambda$ between a current state (flow or heating) and the reference state (no flow or no heating) is related to the refractive index variation, according to the Gladstone-Dale. So, the average air density integrated along the cross section (length L) is obtained by:

$$\langle\rho\rangle = \frac{2}{3\hat{r}}\frac{\lambda}{2\pi L}\Delta\phi_\lambda \quad (11)$$

with $\hat{r} = 0.1516 \times 10^{-3}$ m^3.kg^{-1} at λ=509.7 nm is the specific refractivity of air for the visible range (this value does not change significantly, $\sim 0.0036 \times 10^{-3}$ for wavelengths between 408 nm and 703.4 nm).

4. Experimental results

The optical set-up was tested to analyze the supersonic flow of a small vertical jet, 5.56 mm in diameter at different injection pressures. Fig. 4 shows the digital color holograms for the reference and the measurement with a zoom near the injection area, for a pressure at four bars. The spatial carrier fringes, having a horizontal direction, can be clearly seen. In the zoomed images, one can see the horizontal micro fringes distorted by the flow. Fig. 4 also shows that the field of view is reduced on the right and left sides. This is

due to the rotation of the Wollaston prism which has a limited square aperture (15 mm²). The two orthogonally polarized beams, which were completely separated on the optical paths, interfere when the prism and the analyzer placed in front of the camera are rotated around its optical axis.

Fig. 5 shows the three R-G-B Fourier spectra calculated from the recorded holograms. Since the micro fringes are horizontally oriented, the +1 order is localized along the vertical axis. The filtering is represented by a colored circle and the diameter of the filters are respectively $\Delta u = 0.172\ \mathrm{mm}^{-1}$ for the blue channel, $\Delta u = 0.137\ \mathrm{mm}^{-1}$ for the green and $\Delta u = 0.126\ \mathrm{mm}^{-1}$ for the red one. Thus, the spatial resolutions in the field of view are respectively 25.48 lines/mm, 21.31 lines/mm and 19.6 lines/mm.

Fig. 6 shows the phase map for the blue channel, for the reference and for a pressure at three bars. The spatial carrier frequency remains in the data but will be removed when computing the phase variation between the phase at a given pressure and the reference one.

Fig. 7 exhibits the modulo 2π(a) and the unwrapped (b) phase difference obtained at the same pressure for the green channel. The unwrapped phase scale covers about 15 rad. The average optical thickness is computed from the optical variations according to

$$\langle e \rangle = \frac{\lambda}{2\pi} \Delta\phi_\lambda \tag{12}$$

Fig. 7(c) indicates that the variation between the structure's core and the air outside of the jet is 0.6 μm.

Using the amplitude (a_λ) and phase variation ($\Delta\varphi_\lambda$) computed for each monochromatic hologram, the superposition of the three red, green and blue luminous intensities can be obtained, according to Eq. (13):

$$I_\lambda = a_\lambda.(1 + \cos(\Delta\varphi_\lambda)) \tag{13}$$

Fig. 8(a) shows the superimposition obtained from the phase variations for a pressure at five bars. The color interference fringes are those which should be obtained if an optical technique color holographic interferometry using holographic plates was implemented. In addition, the white fringe on both sides the micro jet indicates where is localized the zero order fringe. The succession of colors that are found on the interferogram in Fig. 8a can be easily interpreted and it also shows the interest of using three wavelengths as the light source of the interferometer. Before recording of the test, if the interferometer is perfectly adjusted, there is no difference in the path difference and the background color is represented by a white color (addition of red, green and blue colors). For information, the colors succession is that can be found in the Newton scale where the central fringe is white. In our case, the interferometer is slightly shifted to get a uniform background color of the first order: brown color, near white color and there is no air density variation in a dynamic flow. Thus, this offset and the colors succession observed in different structures of the jet allows determining the density variation in the areas of compression or expansion of the jet. If the light source of the interferometer is monochromatic, gray levels are observed and there is very difficult to determine the variation of optical path differences. This feature is largely explained by Desse for a oil-film interferometry skin-friction measurement under white light (made by oil film interferometry) [59].

From the phase measurement, the radial distribution of the refractive index is extracted by assuming the flow is axisymmetric. The analysis is performed from the left and right parts of the jet and it is stopped on the jet axis. Further details can be found in reference [60]. The gas density profiles can be calculated in the jet, according to the Gladstone-Dale relation (Eq. (11)) and is shown in Fig. 8(b).

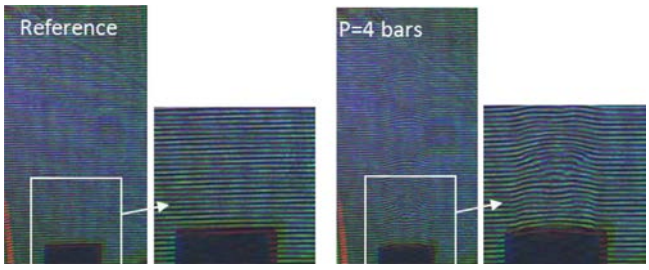

Fig. 4. Digital color holograms for a pressure P=4 bars and zoom in the area near the injection nozzle.

5. Conclusion

In conclusion, an optical setup based on three-wavelength digital holographic interferometry using two Wollaston prisms is presented and includes several advantages compared to others configurations: single crossing of the test section, adjustable spatial carrier frequencies both in amplitude and orientation, quasi-common path interferometer, immunity to external perturbations. The spatial carrier frequencies provided by the Wollaston prisms leads to a Fourier data processing, which means real-time capability for the set-up. The use of three laser wavelengths is useful to determine the zero order

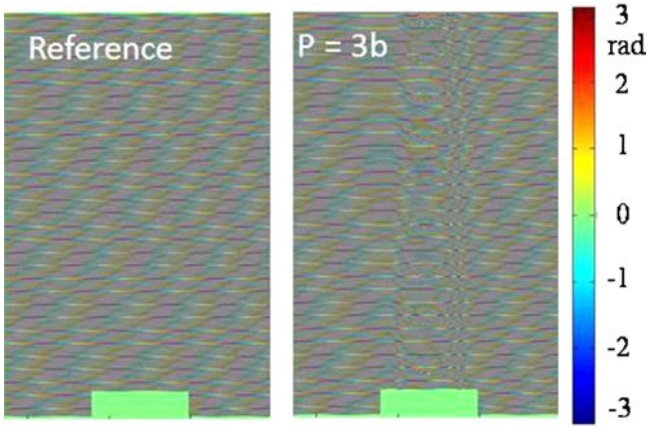

Fig. 6. Modulo 2π phase maps for P=3 bars.

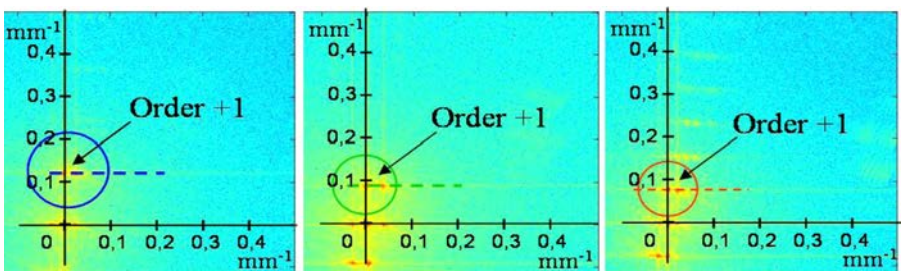

Fig. 5. 2D Fourier Spectra calculated on blue, green and red channels at P=4 bars (unit along the axis: reduced spatial frequency).

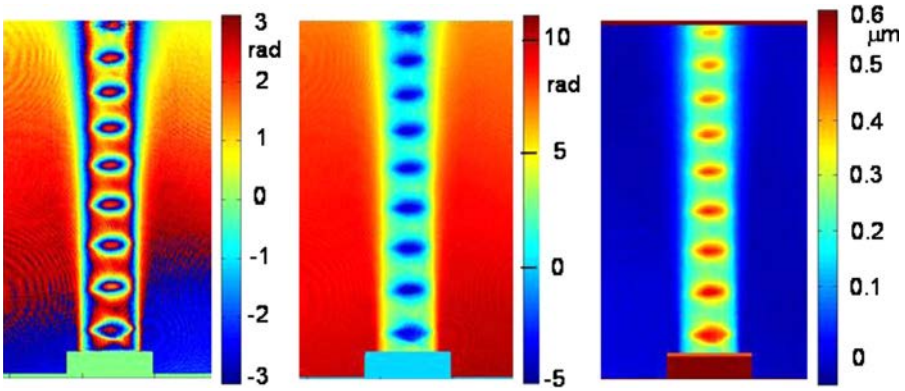

Fig. 7. (a) Modulo 2π phase difference, (b) unwrap phase, (c) optical thickness, for P=3 bars.

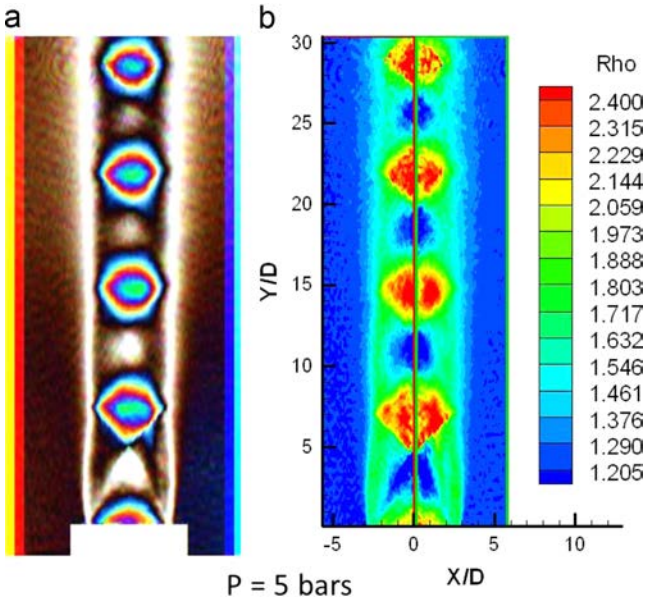

Fig. 8. (a) Color luminous intensity, (b) Radial gas density at P=5 bars.

fringe in the field of view, and as a consequence to visualize regions with no variation in air density. Experimental proof of concept is demonstrated with a micro jet. Assuming the flow is axisymmetric, gas density profiles can be extracted from the phase imaging set-up.

Acknowledgments

This research was partially funded by the French National Agency for Research (ANR) under grant agreement n° ANR 2010 BLAN 0302.

References

[1] Cuche E, Bevilacqua F, Depeursinge C. Digital holography for quantitative phase-contrast imaging. Opt Lett 1999;24:291–3.
[2] Mann C, Yu L, Lo CM, Kim M. High-resolution quantitative phase-contrast microscopy by digital holography. Opt Express 2005;13:8693–8.
[3] Bhaduri B, Pham H, Mir M, Popescu G. Diffraction phase microscopy with white light. Opt Lett 2012;37:1094–6.
[4] Chaniwal V, Singh ASG, Leitgeb RA, Javidi B, Anand A. Quantitative phase-contrast imaging with compact digital holographic microscope employing Lloyd's mirror. Opt Lett 2012;37:5127–9.
[5] Lue N, Kang JW, Hillman TR, Dasari RR, Yaqoob Z. Single-shot quantitative dispersion phase microscopy. Appl Phys Lett 2012;101:084101.
[6] Pham H, Bhaduri B, Ding H, Popescu G. Spectroscopic diffraction phase microscopy. Opt Lett 2012;37:3438–40.
[7] Edwards C, Zhou R, Hwang SW, McKeown SJ, Wang K, Bhaduri B, et al. Diffraction phase microscopy: monitoring nanoscale dynamics in material science. Appl Opt 2014;53:G33–43.
[8] Girshovitz P, Shaked NT. Compact and portable low-coherence interferometer with off-axis geometry for quantitative phase microscopy and nanoscopy. Opt Express 2013;21:5701–14.
[9] Rajshekhar G, Bhaduri B, Edwards C, Zhou R, Goddard LL, Popescu G. Nanoscale topography and spatial light modulator characterization using wide-field quantitative phase imaging. Opt Express 2014;22:3432–8.
[10] Ferraro P, Alferi D, De Nicola S, De Petrocellis L, Finizio A, Pierattini G. Quantitative phase-contrast microscopy by a lateral shear approach to digital holographic image reconstruction. Opt Lett 2006;31:1405–7.
[11] Shaffer E, Moratal C, Magistretti P, Marquet P, Depeursinge C. Label-free second-harmonic phase imaging of biological specimen by digital holographic microscopy. Opt Lett 2010;35:4102–4.
[12] Gabai H, Shaked NT. Dual-channel low-coherence interferometry and its application to quantitative phase imaging of fingerprints. Opt Express 2012;20:26906–12.
[13] Parthasarathy AB, Chu KK, Ford TN, Mertz J. Quantitative phase imaging using a partitioned detection aperture. Opt Lett 2012;37:4062–4.
[14] Mann C, Bingham PR, Paquit VC, Tobin KW. Quantitative phase imaging by three-wavelength digital holography. Opt Express 2008;16:9753–64.
[15] Picart P, Malek M. Complex field recovering from in-line digital holography. Opt Lett 2013;38:3230–2.
[16] Desse JM, Picart P, Tankam P. Digital three-color holographic interferometry for flow analysis. Opt Express 2008;16:5471–80.
[17] Kakue T, Yonesaka R, Tahara T, Awatsuji Y, Kenzo N, Ura S, et al. High-speed phase imaging by parallel phase-shifting digital holography. Opt Lett 2011;36:4131–3.
[18] Desse JM, Tankam P, Picart P. Digital color holography applied to fluid and structural mechanics. Opt Lasers Eng 2012;50:18–28.
[19] Seebacher S, Osten W, Baumbach T, Juptner W. The determination of material parameters of microcomponents using digital holography. Opt Lasers Eng 2011;36:103–26.
[20] Yamaguchi I, Ida T, Yokota M, Yamashita K. Surface shape measurement by phase shifting digital holography with a wavelength shift. Appl Opt 2006;45:7610–6.
[21] Nomura T, Javidi B, Murata S, Nitanai E, Numata T. Polarization imaging of a 3D object by use of on-axis phase-shifting digital holography. Opt Lett 2007;32:481–3.
[22] Morimoto Y, Nomura T, Fjigaki M, Yoneyama S, Takahashi I. Deformation measurement by phase shifting digital holography. Exp Mechanics 2005;45:65–70.
[23] Tankam P, Song Q, Karray M, Li J, Desse JM, Picart P. Real-time three-sensitivity measurements based on three-color digital Fresnel holographic interferometry. Opt Lett 2010;35:2055–7.
[24] Fu Y, Pedrini G, Osten W. Vibration measurement by temporal Fourier analyses of a digital hologram sequence. Appl Opt 2007;46:5719–27.
[25] Leclercq M, Karray M, Isnard V, Gautier F, Picart P. Evaluation of surface acoustic waves on the human skin using quasi-time-averaged digital Fresnel holograms. Appl Opt 2013;52:A136–46.
[26] Joud F, Verpillat F, Laloë F, Atlan M, Hare J, Gross M. Fringe-free holographic measurements of large-amplitude vibrations. Opt Lett 2009;34:3698–700.
[27] Samson B, Verpillat F, Gross M, Atlan M. Video-rate laser Doppler vibrometry by heterodyne holography. Opt Lett 2011;36:1449–51.
[28] Atlan M, Gross M, Desbiolles P, Absil E, Tessier G, Coppey-Moisan M. Heterodyne holographic microscopy of gold particles. Opt Lett 2008;33:500–2.
[29] Müller J, Kebbel V, Jüptner W. Characterization of spatial particle distributions in a spray-forming process using digital holography. Meas Sci Technol 2004;15:706–10.
[30] Pu SL, Allano D, Patte-Rouland B, Malek M, Lebrun D, Cen KF. Particle field characterization by digital in-line holography: 3D location and sizing. Exp Fluids 2005;39:1–9.
[31] Palero V, Lobera J, Arroyo MP. Digital image plane holography (DIPH) for two-phase flow in multiple planes. Exp Fluids 2005;39:397 (06).

[32] Sharma S, Sheoran G, Shakher C. Investigation of temperature and temperature profile in butane torch burner using digital holographic interferometry. Opt Lasers Eng 2012;50:1436–44.
[33] Doleček R, Psota P, Lédl V, Vít T, Václavík J, Kopecký V. General temperature field measurement by digital holography. Appl Opt 2013;52:319–25.
[34] Yamaguchi I, Zhang T. Phase shifting digital holography. Opt Lett 1997;22:1268–70.
[35] Schnars U, Jüptner W. Direct recording of holograms by a CCD target and numerical reconstruction. Appl Opt 1994;33:179–81.
[36] Schnars U, Kreis TM, Jüptner W. Digital recording and numerical reconstruction of holograms: reduction of the spatial frequency spectrum. Opt Eng 1996;35:977–82.
[37] Yamaguchi I, Matsumura T, Kato JI. Phase-shifting color digital holography. Opt Lett 2002;27:1108–10.
[38] Kato JI, Yamaguchi I, Matsumura T. Multicolor digital holography with an achromatic phase shifter. Opt Lett 2002;27:1403–5.
[39] Demoli N, Vukicevic D, Torzynski M. Dynamic digital holographic interferometry with three wavelengths. Opt Express 2003;11:767–74.
[40] Javidi B, Ferraro P, Hong S, De Nicola S, Finizio A, Alfieri D, et al. Three-dimensional image fusion by use of multiwavelength digital holography. Opt Lett 2005;30:144–6.
[41] Alfieri D, Coppola G, De Nicola S, Ferraro P, Finizio A, Pierattini G, et al. Method for superposing reconstructed images from digital holograms of the same object recorded at different distance and wavelength. Opt Commun 2006;260:113–6.
[42] Zhao J, Jiang H, Di J. Recording and reconstruction of a color holographic image by using digital lensless Fourier transform holography. Opt. Express. 2008;16:2514–9.
[43] Yeom S, Javidi B, Ferraro P, Alfieri D, De Nicola S, Finizio A. Three-dimensional color object visualization and recognition using multi-wavelength computational holography. Opt Express 2007;15:9394–402.
[44] Ferraro P, Grilli S, Miccio L, Alfieri D, De Nicola S, Finizio A, et al. Full color 3-D imaging by digital holography and removal of chromatic aberrations. J Disp Tech 2008;4:97–100.
[45] Picart P, Tankam P, Mounier D, Peng Z, Li J. Spatial bandwidth extended reconstruction for digital color Fresnel holograms. Opt Express 2009;17:9145–56.
[46] Leclercq M, Picart P. Method for chromatic error compensation in digital color holographic imaging. Opt Express 2013;21:26456–67.
[47] Xia P, Shimozato Y, Ito Y, Tahara T, Kakue T, Awatsuji Y, et al. Improvement of color reproduction in color digital holography by using spectral estimation technique. Appl Opt 2011;50:H177–82.
[48] Garcia-Sucerquia J. Color lensless digital holographic microscopy with micrometer resolution. Opt Lett 2012;37:1724–6.
[49] Ito Y, Shimozato Y, Xia P, Tahara T, Kakue T, Awatsuji Y, et al. Four-wavelength color digital holography. J Display Technol 2012;8:570–6.
[50] Kowalczyk A, Bieda M, Makowski M, Sypek M, Kolodziejczyk A. Fiber-based real-time color digital in-line holography. Appl Opt 2013;52:4743–8.
[51] Kim M. Full color natural light holographic camera. Opt Express 2013;21:9636–42.
[52] Yu L, Kim M. Full-color three-dimensional microscopy by wide-field optical coherence tomography. Opt Express 2004;12:6632–41.
[53] Kiire T, Barada D, Sugisaka JI, Hayasaki Y, Yatagai T. Color digital holography using a single monochromatic imaging sensor. Opt Lett 2012;37:3153–5.
[54] Parshall D, Kim MK. Digital holographic microscopy with dual-wavelength phase unwrapping. Appl Opt 2006;45:451–9.
[55] Kühn J, Colomb T, Montfort F, Charrière F, Emery Y, Cuche E, et al. Real-time dual-wavelength digital holographic microscopy with a single hologram acquisition. Opt Express 2007;15:7231–42.
[56] Jafarfard MR, Moon S, Tayebi B, Kim DY. Dual-wavelength diffraction phase microscopy for simultaneous measurement of refractive index and thickness. Opt Lett 2014;39:2908–11.
[57] Gontier G, Carr P, Henon G. Sur un dispositif d'interférométrie différentielle permettant d'orienter arbitrairement les franges par rapport à la direction du décalage des faisceaux. Compte-rendu Acad Sci 1966;262:674–7.
[58] Li J, Tankam P, Peng Z, Picart P. Digital holographic reconstruction of large objects using a convolution approach and adjustable magnification. Opt Lett 2009;34:572–4.
[59] Desse JM. Oil-film interferometry skin-friction measurement under white light. AIAA J 2003;41:2468–77.
[60] Rodriguez O, Desse JM, Pruvost J. Interaction between a supersonic hot jet and a coaxial supersonic flow. Aerospace Sci Technol 1997;11:369–79.